



Published in final edited form as:

Med Dosim. 2019 ; 44(4): e64–e70. doi:10.1016/j.meddos.2019.01.002.

Dose Evaluation of MRI-based Synthetic CT Generated Using a Machine Learning Method for Prostate Cancer Radiotherapy

Ghazal Shafai-Erfani, Tonghe Wang, Yang Lei, Sibotian, Preteah Patel, Ashesh B. Jani, Walter J. Curran, Tian Liu, Xiaofeng Yang

Department of Radiation Oncology and Winship Cancer Institute, Emory University, Atlanta, GA 30322

Abstract

Purpose: MRI-only radiotherapy treatment planning is attractive since MRI provides superior soft tissue contrast over CTs, without the ionizing radiation exposure. However, it requires the generation of a synthetic CT (SCT) from MRIs for patient setup and dose calculation. In this study, we aim to investigate the accuracy of dose calculation in prostate cancer radiotherapy using SCTs generated from MRIs using our learning-based method.

Materials and Methods: We retrospectively investigated a total of 17 treatment plans from 10 patients, each having both planning CTs (pCT) and MRIs acquired before treatment. The SCT was registered to the pCT for generating SCT-based treatment plans. The original pCT-based plans served as ground truth. Clinically-relevant dose volume histogram (DVH) metrics were extracted from both ground truth and SCT-based plans for comparison and evaluation. Gamma analysis was performed for the comparison of absorbed dose distributions between SCT- and pCT-based plans of each patient.

Results: Gamma analysis of dose distribution on pCT and SCT within 1%/1 mm at 10% dose threshold showed greater than 99% pass rate. The average differences in dose volume histogram (DVH) metrics for planning target volumes (PTVs) were less than 1%, and similar metrics for organs at risk (OAR) were not statistically different.

Conclusion: The SCT images created from MR images using our proposed machine learning method are accurate for dose calculation in prostate cancer radiation treatment planning. This study also demonstrates the great potential for MRI to completely replace CT scans in the process of simulation and treatment planning. However, MR images are needed to further analyze geometric distortion effects. Digitally reconstructed radiograph (DRR) can be generated within our method, and their accuracy in patient setup needs further analysis.

Keywords

MRI; Treatment planning; SCT

Reprint request to Dr. Xiaofeng Yang, Department of Radiation Oncology and Winship Cancer Institute, Emory University, Atlanta, GA 30322, USA. xiaofeng.yang@emory.edu (X. Yang).

Publisher's Disclaimer: This is a PDF file of an unedited manuscript that has been accepted for publication. As a service to our customers we are providing this early version of the manuscript. The manuscript will undergo copyediting, typesetting, and review of the resulting proof before it is published in its final citable form. Please note that during the production process errors may be discovered which could affect the content, and all legal disclaimers that apply to the journal pertain.

INTRODUCTION

There is a growing interest in incorporating magnetic resonance imaging (MRI) in radiation therapy¹ owing to its superior soft tissue contrast over computed tomography (CT), which is crucial for target and OAR delineation.^{2,3} This is particularly important for intensity modulated radiation therapy (IMRT), due to the sharp falloff outside the target volume.² Since CT images provide electron density maps for dose calculation and reference images for setup positioning, MR images, when used for treatment planning are first fused to the reference CT via a rigid or deformable registration.^{1,4}

Image registration, however, introduces registration uncertainty,⁵ which stems from challenges of image registration due to (1) actual geometrical differences at the time of image acquisition, and (2) modality related geometrical distortions. Actual geometrical differences result from differences in patient setup, internal organ motion, changes in patient anatomy at the time of the two image acquisitions (organ swelling, changes in weight). Registration uncertainty is reported to range from 0.5 to 3.5 mm,^{6–9} and results in uncertainty in contours which consecutively propagates throughout the entire treatment course, resulting in a systematic error. Since MR acquisition is already standard practice in radiation therapy workflow, elimination of CT acquisition subsequently the respective cost will simplify the workflow, as well as a non-negligible concomitant dose received by the patient during CT image acquisition.¹⁰ The latter is of particular importance for pediatric patients, especially those undergoing multiple scans during their treatment.¹¹ Moreover, with the rise of MRI-guided treatment techniques, such as MRI-LINACs,^{12–16} eliminating CT acquisition from the patient care path is increasingly appealing.

The main challenge of MRI-only treatment planning is the fact that MRI signal intensity correlates with proton density and tissue relaxation properties rather than electron density which is crucial for dose calculation.^{7,17} Moreover, lack of signal from cortical bone in conventional MRI poses a dilemma for generating the positional verification reference images that are needed for image-guided radiation therapy (IGRT). To overcome these obstacles, three main approaches^{4,18} have been proposed to estimate tissue attenuation properties using MRI: (1) voxel-based,^{19,20} (2) atlas-based,^{21–24} (3) bulk assignment-based techniques.^{17,25–29} The MR-based tissue attenuation maps generated using the above methods are referred to as Synthetic CT (SCT). However, voxel based techniques require unconventional MR sequences which are not available for every patient. The accuracy of atlas-based and bulk assignment-based methods is constrained by the limitations in classification and distinction between air and bone regions.

With recent developments brought about by machine learning techniques, novel methods to generate MRI-based SCT with promising accuracy have been proposed.^{30–32} These methods use a large number of pairs of registered planning CT (pCT) and MR images of each patient, with which the model learns the conversion between the MR signal and attenuation coefficient in CT. After the training phase, the algorithm uses MR images to predict the corresponding SCT. Recently, our group has developed a method to obtain SCTs from MR

images^{33,34} using machine learning with an auto-context model, with promising results for brain stereotactic radiosurgery.³⁵

In this retrospective study, we present the accuracy of our method^{33,34} in dose calculation for prostate Volumetric Arc Therapy (VMAT) planning. We compare dose volume histogram (DVH) endpoints for clinically relevant structures, and dose distributions obtained from SCT against those from the ground truth pCT.

METHODS AND MATERIALS

We initially built a set of paired training MRI and CT images. The CT images served as the regression target of the MRI. We then performed preprocessing by removing uninformative regions and reducing noise, followed by aligning MRI and CT images with a rigid registration. The synthesis of CT images consists of two major stages: the training stage and the synthesis stage. In the training stage, we first extracted anatomical features on voxel, sub-region and whole-patch levels from each MR image, identified the most salient and informative features and utilize them together with the corresponding CT image to train an initial structured random forest based on an integrated auto-context model (ACM).^{34,36} We then used the resulting forest to generate the SCT image for each MR image in the training set, leading to an initial set of predictions/generations. Together with the features from original CT images, we further extracted context features from the predicted CT images to train a new structured random forest to perform another prediction. By repeating this process until convergence, we obtained a sequence of trained forests. In the synthesis stage, we extracted features from the new MR image (target) and fed them into the trained forests for the CT image generation. Figure 1 shows a schematic view of our proposed method.

10 prostate cancer patients who were treated with external beam radiation therapy at a single institution were randomly selected. Standard care CT and MR images were acquired. MR images were acquired using a Siemens AVANTO MRI scanner with $1.0 \times 1.0 \times 2.0 \text{ mm}^3$ voxel size (TR/TE: 1000/123 ms) and CTs were captured with a Siemens SOMATOM Definition AS CT scanner with $1.0 \times 1.0 \times 2.0 \text{ mm}^3$ voxel size. 7 patients were treated with an initial plan that was followed by a boost, which resulted in total of 17 plans. All patients, with the exception of one patient who was prescribed 70 Gy, were prescribed a total dose of 79.2 Gy. Because treatments were divided into two (initial and boost) plans, the dose per plan ranged from 34.2 to 79.2 Gy.

In order to evaluate the performance of the SCT images, we compared the dose distribution calculated on the SCT against that of the pCT. All plans were created in Eclipse 13.6 (Varian Medical Systems, Palo Alto, CA) using VMAT technique, using 10 MV photons with a 2.5mm dose grid. We kept all plan parameters the same, in order to keep the comparison monovariant. Due to uncertainties associated with reproducibility of patient setup, as well as anatomical changes and/or organ motion that might have occurred between the two image acquisitions, deformable registration was performed using commercial image registration software, Velocity AI 3.2.1 (Varian Medical Systems, Palo Alto, CA), to align SCT images obtained from MRIs to the pCT. The original treatment plan was duplicated onto SCT

volumes and doses were recalculated using the same algorithm (analytical anisotropic algorithm, AAA), grid size (0.1 cm) and HU calibration.

Dose distributions obtained from SCT plans were qualitatively compared against those derived from pCTs. Clinically relevant DVH endpoints were compared for PTV and relevant OARs. Gamma analysis using 1%/1mm criteria was performed on the axial, sagittal, and coronal planes at isocenter to compare dose distributions computed on SCTs and pCTs.

RESULTS

Figure 2 presents a side-by-side view of pCT, SCT, and MR images obtained from a single patient, shown at the same window and level. Qualitatively, the SCT images maintain image quality and structural details. However, structural discrepancies between the two images occur in small volumes in areas of bone and air, and the SCT images overall appears slightly blurred.

Figures 3(a1-c1) and 3(a2-c2) show the dose color wash for pCT and SCT-based plans in axial, sagittal, and coronal views. Qualitatively, the two plans are very similar. Figure 3(a3-c3) shows the dose difference map in each view. As seen, the differences are minor for the majority of the volume, and the maximum difference occurs at the external outline of the body. Dose profiles along the two axes for each plane are presented in Figures 3(a4-c4, a5-c5), and further demonstrate that dose distribution based on pCT and SCT images are in accord. DVH curves of PTV and relevant OARs for are presented in Figure 4 as an example. The close agreement of DVHs parameters derived from SCT and the pCT plans shows minimal dose difference between the two; plan quality is nearly identical for the 2 cases.

Differences in PTVs and OARs DVH metrics for of the 17 plans are presented by boxplots in Figure 5 and Figure 6, respectively. The central line in each box shows the median, and the yellow and gray bars present 25th and 75th percentiles, respectively. The whiskers extend to the most extreme data points excluding the outliers, which are shown individually using the 'x' symbol. Differences in DVH metrics for all 17 plans are summarized in Table I. Standard deviation (STD), and the p-values calculated with null hypothesis of zero dose difference between SCT and pCT are presented. For all PTV metrics, the average difference among the 17 plans is less than 0.1 Gy or 0.3%; and p-values for all metrics are greater than 0.05, confirming high accuracy of dose calculated based on our method. Additionally, gamma analysis using 1% 1 mm criteria on axial, sagittal, and coronal plans at isocenter for all plans shows a passing rate of over 99%.

Another important challenge in MRI-based planning is the feasibility of generating digitally reconstructed radiograph (DRR) for patient setup. Figure 7 shows DRRs generated from the pCT (a) and the SCT (b). Visually, the images show good agreement, although errors appear in bone detection.

DISCUSSION

In this study, we evaluated the accuracy of dose calculations of prostate VMAT plans using SCT images generated from MR images by our machine-learning-based method. Side-by-

side comparison of the two reveals similar image contrast and good agreement in dose distribution. However, the image quality of the original pCT was better than that of the SCTs. Since contouring was performed on MR images and SCTs are used merely for dose calculation purposes, contouring accuracy in SCT and pCT were the same. Our statistical analysis of DVH endpoints for 17 plans for 10 patients showed that the average differences in DVH endpoints of PTVs and OARs were not statistically different at significance level of 0.05. High accuracy of dose calculation on SCT is further supported by the gamma analysis at 1% 1 mm pass rate of 100%, which is comparable with previously published results of 99.9% pass rate at 2%, 1 mm.³⁷ Relative dose difference in several DVH endpoints for the PTV was less than 1%. The above quantitative results show the accuracy of dose calculation for prostate VMAT using our method is sufficient to replace pCTs. The dose calculation errors based on SCTs were mainly at the external body contour, which was generated based on the MR images. This can originate either from registration uncertainty or from errors in detection of the interface of the body which requires accurate detection of air. Body contour is defined based on the pCT. However, SCT relies on MR images to detect the interface of air and tissue and assign HU values accordingly. Any error in HU values will result in differences dose distribution.

In this study, MR images available to us had limited FOV. In order to resolve the truncation issue in this dosimetric comparison, the surrounding tissues which fell outside the MRI FOV were adopted from the pCT to construct complete anatomy of the patient which fell within pCT image. The SCT was constructed by interpolation into the same voxel size as the pCT. One might argue that the excellent agreement between dose distributions based on composite SCTs and the pCTs is due to the shared information between the two. Though this is a valid concern, this issue affected less than 10% of the volume of the SCT. Therefore, the agreement between dose distributions is based on different image information sources. Yet, the fact that the two images are patched suggests that our SCTs inherently contain image registration errors. Though this negates one of the most attractive advantages of MRI-based planning, our results provide evidence for proof of concept.

Our next step is to obtain MR images with larger FOVs to better test our method of dose calculation based on SCTs. Larger FOVs on MR images however introduce complex image distortion errors. It is important to evaluate the magnitude of discrepancies related to these errors. Another question is whether our machine learning algorithm is capable of detecting and rectifying distortions. Assessment of geometric distortions associated with MR images over a large FOV, and the performance and efficiency of our machine-learning algorithm in detecting and rectifying for such geometric distortions need to be evaluated, and performance of our machine-learning algorithm in recognizing and rectifying for such distortions needs to be tested. The efficacy of the DRRs generated by this method for patient setup need to be evaluated using a phantom. Another important issue is the accuracy of this method in patient positioning. Though generation of DRRs is possible (shown in Figure 7), their efficacy in reproducible positioning of the patient was not studied. Phantom studies are needed to provide us with quantitative understanding of the distortion and setup errors. Another interesting question to evaluate the feasibility of our MRI-based SCT for dose calculation for proton therapy.

CONCLUSIONS

We investigated the dose calculation accuracy of SCT images generated from routine MRIs for MRI-based prostate cancer radiotherapy using our novel machine learning-based method. Quantitative results based on 17 SCT- and pCT-based prostate plans show no significant differences in DVH endpoints for PTVs and relevant OARs. This demonstrates that the reported method is capable of reliably generating SCT images from MR images and provides dose calculation of comparable accuracy to the standard CTs used for prostate cancer treatment planning. The image accuracy and dosimetric agreement between synthetic and planning CTs warrant further development of an MRI-only workflow for prostate cancer radiotherapy. This would potentially eliminate CT acquisition and subsequently the respective cost, simplify the workflow, eliminate registration uncertainties.¹⁰

ACKNOWLEDGMENTS

This research is supported in part by the National Cancer Institute of the National Institutes of Health under Award Number R01CA215718 (XY), the Department of Defense (DoD) Prostate Cancer Research Program (PCRP) Award W81XWH-13-1-0269 (XY), DoD W81XWH-17-1-0438 (TL) and W81XWH-17-1-0439 (AJ) and Dunwoody Golf Club Prostate Cancer Research Award (XY), a philanthropic award provided by the Winship Cancer Institute of Emory University.

REFERENCES

1. Nyholm T, Jonsson J. Counterpoint: Opportunities and challenges of a magnetic resonance imaging-only radiotherapy work flow. *Seminars in radiation oncology*. 2014;24(3):175–180. [PubMed: 24931088]
2. Dirix P, Haustermans K, Vandecaveye V. The value of magnetic resonance imaging for radiotherapy planning. *Seminars in radiation oncology*. 2014;24(3):151–159. [PubMed: 24931085]
3. Khoo VS, Joon DL. New developments in MRI for target volume delineation in radiotherapy. *The British journal of radiology*. 2006;79:S2–15. [PubMed: 16980682]
4. Johnstone E, Wyatt JJ, Henry AM, et al. Systematic Review of Synthetic Computed Tomography Generation Methodologies for Use in Magnetic Resonance Imaging-Only Radiation Therapy. *International Journal of Radiation Oncology Biology Physics*. 2018;100(1):199–217.
5. Fraass BA, McShan DL, Diaz RF, et al. Integration of magnetic resonance imaging into radiation therapy treatment planning: i. technical considerations. *International Journal of Radiation Oncology*Biophysics*. 1987;13(12):1897–1908.
6. Demol B, Boydev C, Korhonen J, Reynaert N. Dosimetric characterization of MRI-only treatment planning for brain tumors in atlas-based pseudo-CT images generated from standard T1-weighted MR images. *Medical Physics*. 2016;43(12):6557–6568. [PubMed: 27908187]
7. Nyholm T, Nyberg M, Karlsson MG, Karlsson M. Systematisation of spatial uncertainties for comparison between a MR and a CT-based radiotherapy workflow for prostate treatments. *Radiat Oncol*. 2009;4:1–9. [PubMed: 19138400]
8. Andreasen D, Van Leemput K, Hansen RH, Andersen JAL, Edmund JM. Patch-based generation of a pseudo CT from conventional MRI sequences for MRI-only radiotherapy of the brain. *Medical Physics*. 2015;42(4):1596–1605. [PubMed: 25832050]
9. Ulin K, Urie MM, Cherlow JM. Results of a Multi-Institutional Benchmark Test for Cranial CT/MR Image Registration. *International Journal of Radiation Oncology Biology Physics*. 2010;77(5):1584–1589.
10. Edmund JM, Nyholm T. A review of substitute CT generation for MRI-only radiation therapy. *Radiation Oncology*. 2017;12(1):28. [PubMed: 28126030]
11. Schmidt MA, Payne GS. Radiotherapy planning using MRI. *Physics in Medicine & Biology*. 2015;60(22):R323. [PubMed: 26509844]

12. Lagendijk JJW, Raaymakers BW, van Vulpen M. The Magnetic Resonance Imaging-Linac System. *Seminars in radiation oncology*. 2014;24(3):207–209. [PubMed: 24931095]
13. Kupelian P, Sonke J-J. Magnetic Resonance–Guided Adaptive Radiotherapy: A Solution to the Future. *Seminars in radiation oncology*. 2014;24(3):227–232. [PubMed: 24931098]
14. Rai R, Kumar S, Batumalai V, et al. The integration of MRI in radiation therapy: collaboration of radiographers and radiation therapists. *Journal of Medical Radiation Sciences*. 2017;64(1):61–68. [PubMed: 28211218]
15. Lagendijk JJW, Raaymakers BW, Raaijmakers AJE, et al. MRI/linac integration. *Radiotherapy and Oncology*. 2008;86(1):25–29. [PubMed: 18023488]
16. Fallone BG, Murray B, Rathee S, et al. First MR images obtained during megavoltage photon irradiation from a prototype integrated linac-MR system. *Medical Physics*. 2009;36(6):2084–2088. [PubMed: 19610297]
17. Jonsson JH, Karlsson MG, Karlsson M, Nyholm T. Treatment planning using MRI data: an analysis of the dose calculation accuracy for different treatment regions. *Radiation Oncology*. 2010;5(1):62. [PubMed: 20591179]
18. Maspero M, Seevinck PR, Schubert G, et al. Quantification of confounding factors in MRI-based dose calculations as applied to prostate IMRT. *Physics in medicine and biology*. 2017;62(3):948–965. [PubMed: 28076338]
19. Jonsson JH, Johansson A, Söderström K, Askund T, Nyholm T. Treatment planning of intracranial targets on MRI derived substitute CT data. *Radiotherapy and Oncology*. 2013;108(1):118–122. [PubMed: 23830190]
20. Kapanen M, Tenhunen M. T1/T2*-weighted MRI provides clinically relevant pseudo-CT density data for the pelvic bones in MRI-only based radiotherapy treatment planning. *Acta Oncologica*. 2013;52(3):612–618. [PubMed: 22712634]
21. Sjölund J, Forsberg D, Andersson M, Knutsson H. Generating patient specific pseudo-CT of the head from MR using atlas-based regression. *Physics in Medicine & Biology*. 2015;60(2):825. [PubMed: 25565133]
22. Dowling JA, Lambert J, Parker J, et al. An Atlas-Based Electron Density Mapping Method for Magnetic Resonance Imaging (MRI)-Alone Treatment Planning and Adaptive MRI-Based Prostate Radiation Therapy. *International Journal of Radiation Oncology Biology Physics*. 2012;83(1):e5–e11.
23. Uh J, Merchant TE, Li Y, Li X, Hua C. MRI-based treatment planning with pseudo CT generated through atlas registration. *Medical Physics*. 2014;41(5):051711. [PubMed: 24784377]
24. Andreassen D, Van Leemput K, Edmund JM. A patch-based pseudo-CT approach for MRI-only radiotherapy in the pelvis. *Medical Physics*. 2016;43(8):4742–4752. [PubMed: 27487892]
25. Lee YK, Bollet M, Charles-Edwards G, et al. Radiotherapy treatment planning of prostate cancer using magnetic resonance imaging alone. *Radiotherapy and oncology : journal of the European Society for Therapeutic Radiology and Oncology*. 2003;66(2):203–216. [PubMed: 12648793]
26. Lambert J, Greer PB, Menk F, et al. MRI-guided prostate radiation therapy planning: Investigation of dosimetric accuracy of MRI-based dose planning. *Radiotherapy and Oncology*. 2011;98(3):330–334. [PubMed: 21339009]
27. Korsholm ME, Waring LW, Edmund JM. A criterion for the reliable use of MRI-only radiotherapy. *Radiation Oncology*. 2014;9(1):16. [PubMed: 24405515]
28. Chin AL, Lin A, Anamalayil S, Teo B-KK. Feasibility and limitations of bulk density assignment in MRI for head and neck IMRT treatment planning. *Journal of Applied Clinical Medical Physics*. 2014;15(5):100–111.
29. Doemer A, Chetty IJ, Glide-Hurst C, et al. Evaluating organ delineation, dose calculation and daily localization in an open-MRI simulation workflow for prostate cancer patients. *Radiation Oncology*. 2015;10(1):37. [PubMed: 25889107]
30. Aouadi S, Vasic A, Paloor S, et al. Sparse patch-based method applied to mri-only radiotherapy planning. *Physica Medica*. 2016;32:309.
31. Huynh T, Gao Y, Kang J, et al. Estimating CT Image From MRI Data Using Structured Random Forest and Auto-Context Model. *IEEE transactions on medical imaging*. 2016;35(1):174–183. [PubMed: 26241970]

32. Han X MR-based synthetic CT generation using a deep convolutional neural network method. *Med Phys.* 2017;44(4):1408–1419. [PubMed: 28192624]
33. Yang X, Lei Y, Shu H-K, et al. Pseudo CT estimation from MRI using patch-based random forest. Paper presented at: SPIE Medical Imaging2017.
34. Yang X, Lei Y, Shu HKG, et al. A Learning-Based Approach to Derive Electron Density from Anatomical MRI for Radiation Therapy Treatment Planning. *International Journal of Radiation Oncology Biology Physics.* 2017;99(2):S173–S174.
35. Wang T, Manohar N, Lei Y, et al. MRI-based treatment planning for brain stereotactic radiosurgery: Dosimetric validation of a learning-based pseudo-CT generation method. *Medical dosimetry : official journal of the American Association of Medical Dosimetrists.* 2018.
36. Lei Y, Shu HK, Tian S, et al. Magnetic resonance imaging-based pseudo computed tomography using anatomic signature and joint dictionary learning. *Journal of medical imaging (Bellingham, Wash).* 2018;5(3):034001.
37. Siversson C, Nordström F, Nilsson T, et al. Technical Note: MRI only prostate radiotherapy planning using the statistical decomposition algorithm. *Medical Physics.* 2015;42(10):6090–6097. [PubMed: 26429284]

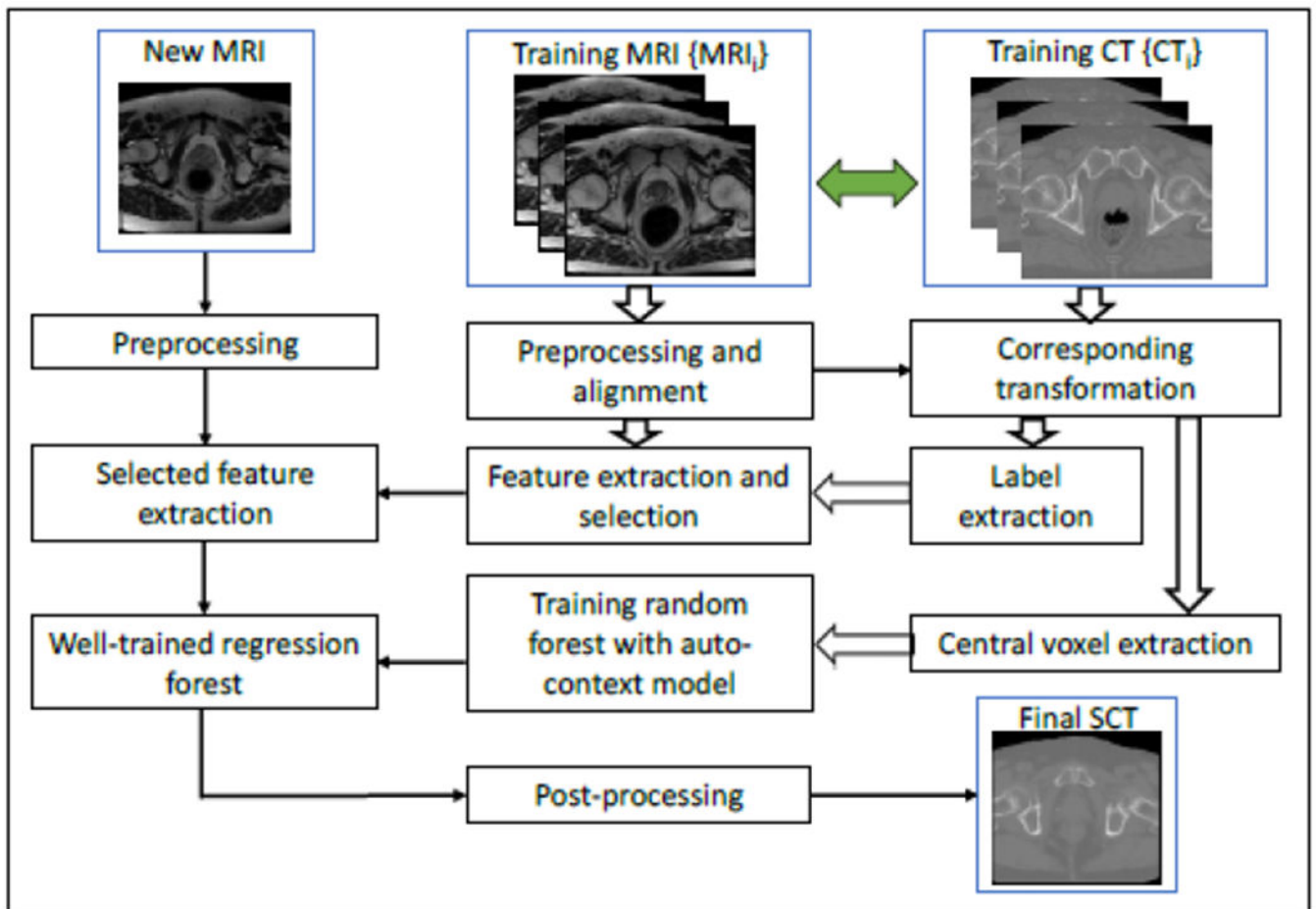


Figure 1. Schematic flow chart of the proposed algorithm for MRI-based synthetic CT (SCT) generation.

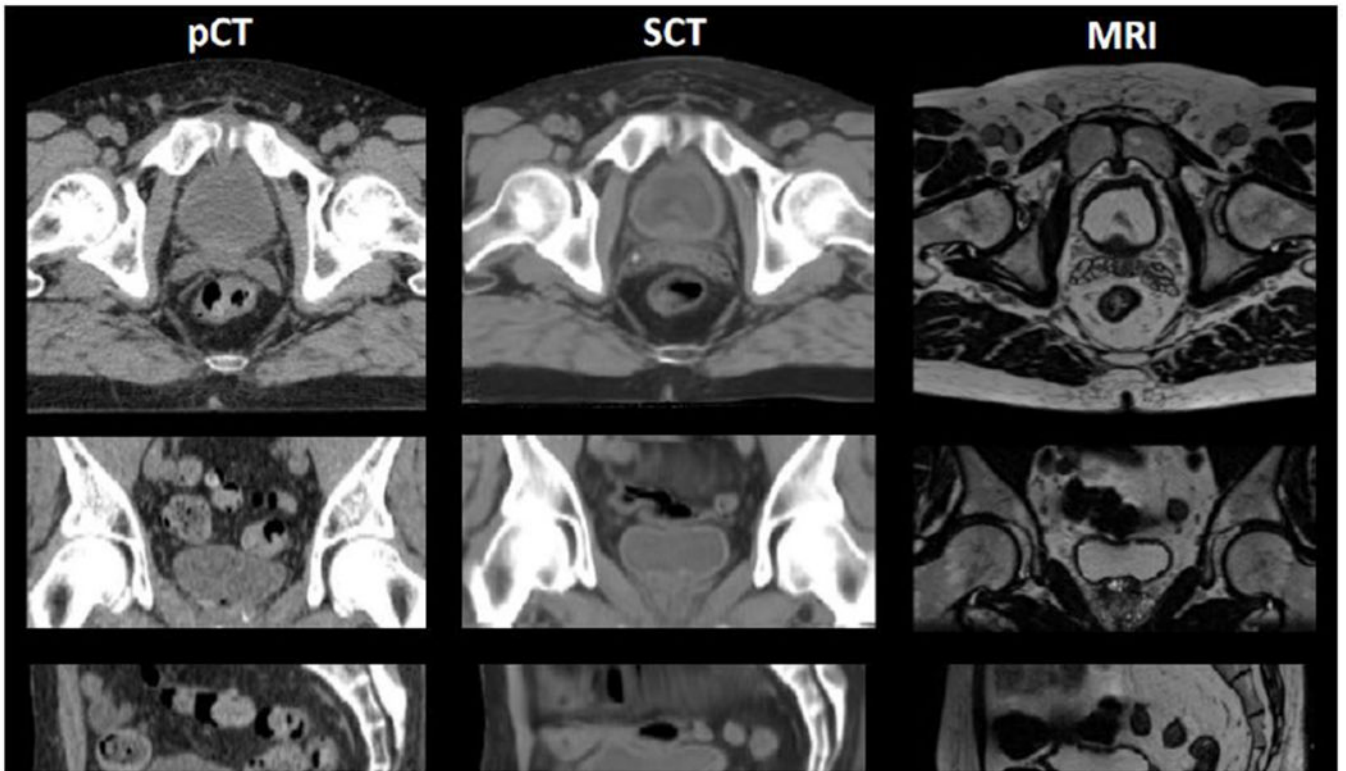


Figure 2.

The axial, sagittal, and coronal view of CT images of one of the 10 patients. Columns (a), (b), and (c) show the pCT images (from simulation), SCT images after a deformable SCT-pCT registration, and MR images, respectively. The red contours indicate PTVs. Display window: $[-160, 240]$ HU.

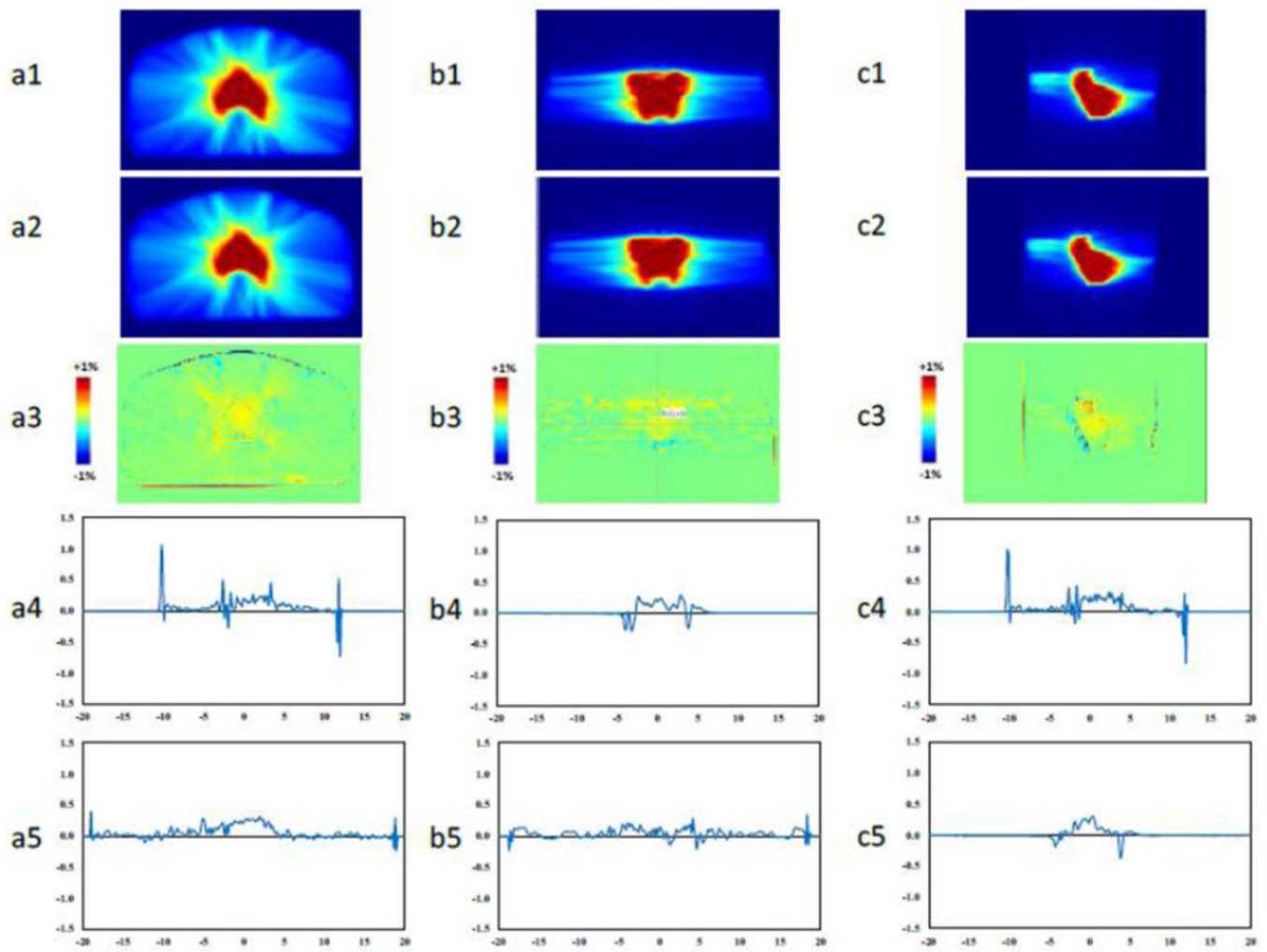


Figure 3.

Dose color washes of (1) pCT and (2) SCT plans for the patient shown in Figure 2. Dose difference maps between (1) and (2) are shown in (3). Dose percentage difference profiles on the 2 axes in each plane are depicted in (4) and (5). a, b, and c are axial, sagittal, and coronal views, respectively.

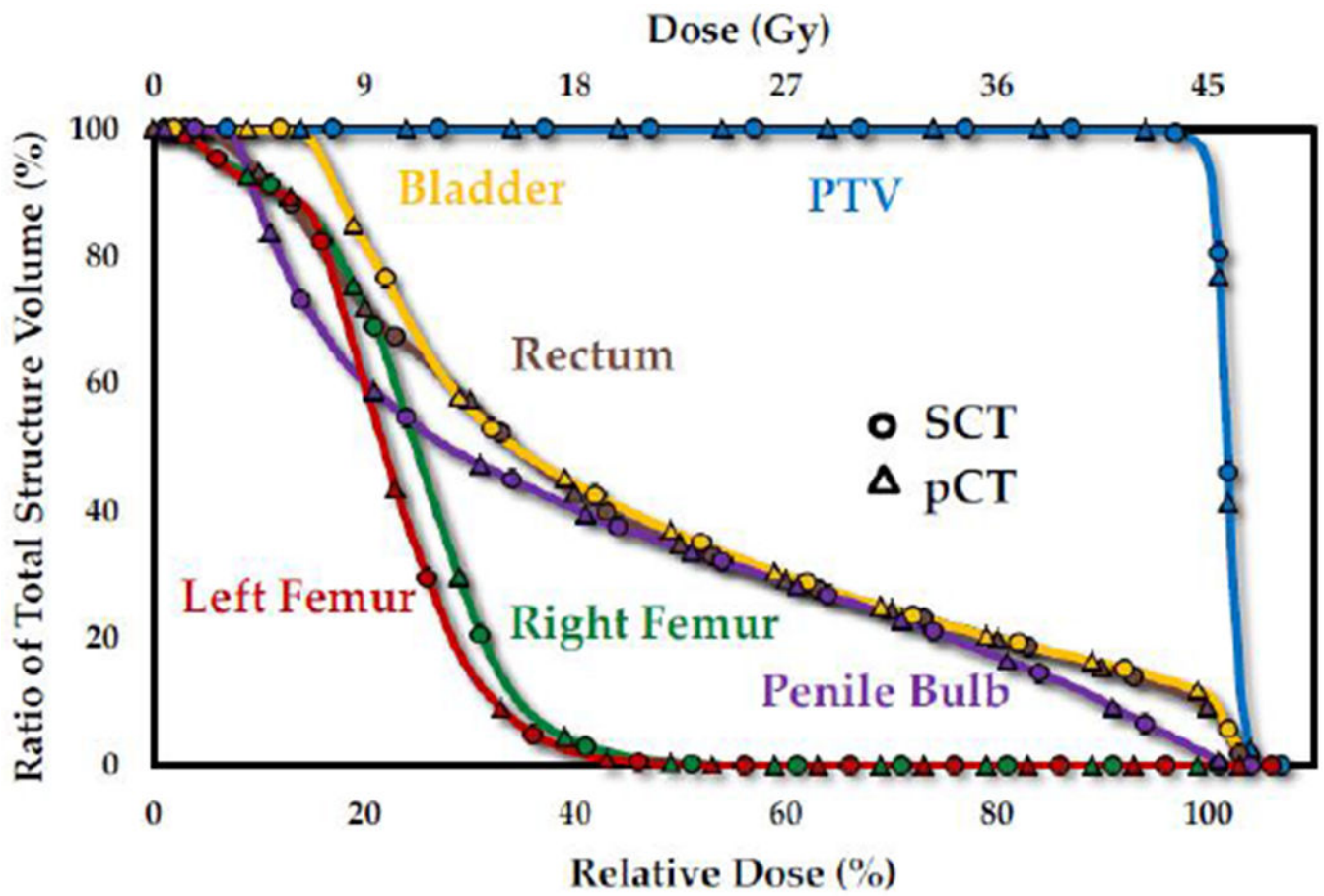


Figure 4. DVH curves for the PTV, bladder, rectum, penile bulb, left and right femoral heads of the patient presented in Figure 2

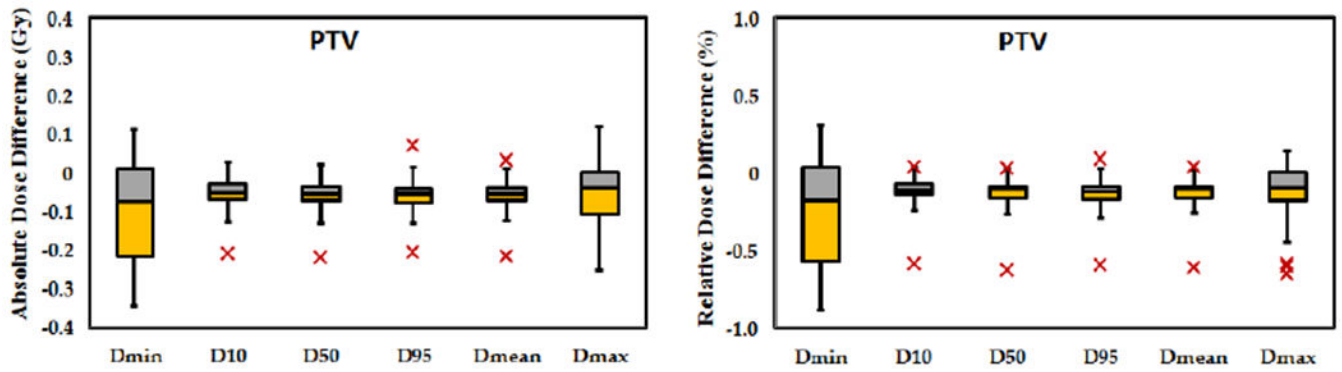


Figure 5.

Statistical distribution of a) absolute and b) relative dose distribution at DVH endpoints for PTVs of all 17 plans. The central mark indicates the median. The yellow and gray bars indicate the second and third quartiles, respectively. The whiskers extend to the most extreme data points not considered outliers, outliers are plotted individually as 'x'

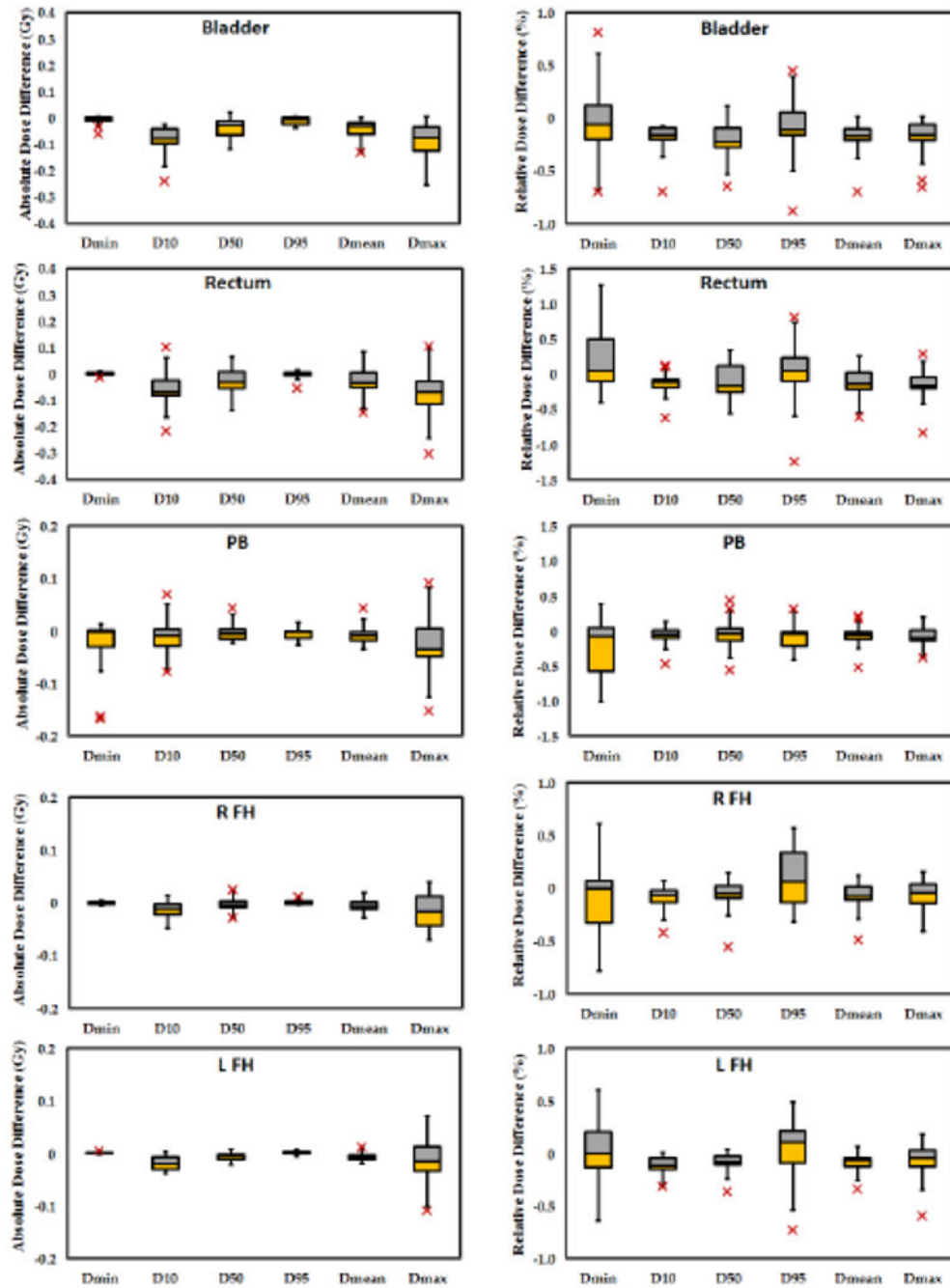


Figure 6. Statistical distribution of column a) absolute and column b) relative dose distribution at DVH endpoints for OARs of all 17 plans. The central mark indicates the median. The yellow and gray bars indicate the second and third quartiles, respectively. The whiskers extend to the most extreme data points not considered outliers, and the outliers are plotted individually using the ‘x’ symbol. (PB - penile bulb, LFH - left femoral head, RFH - right femoral head)

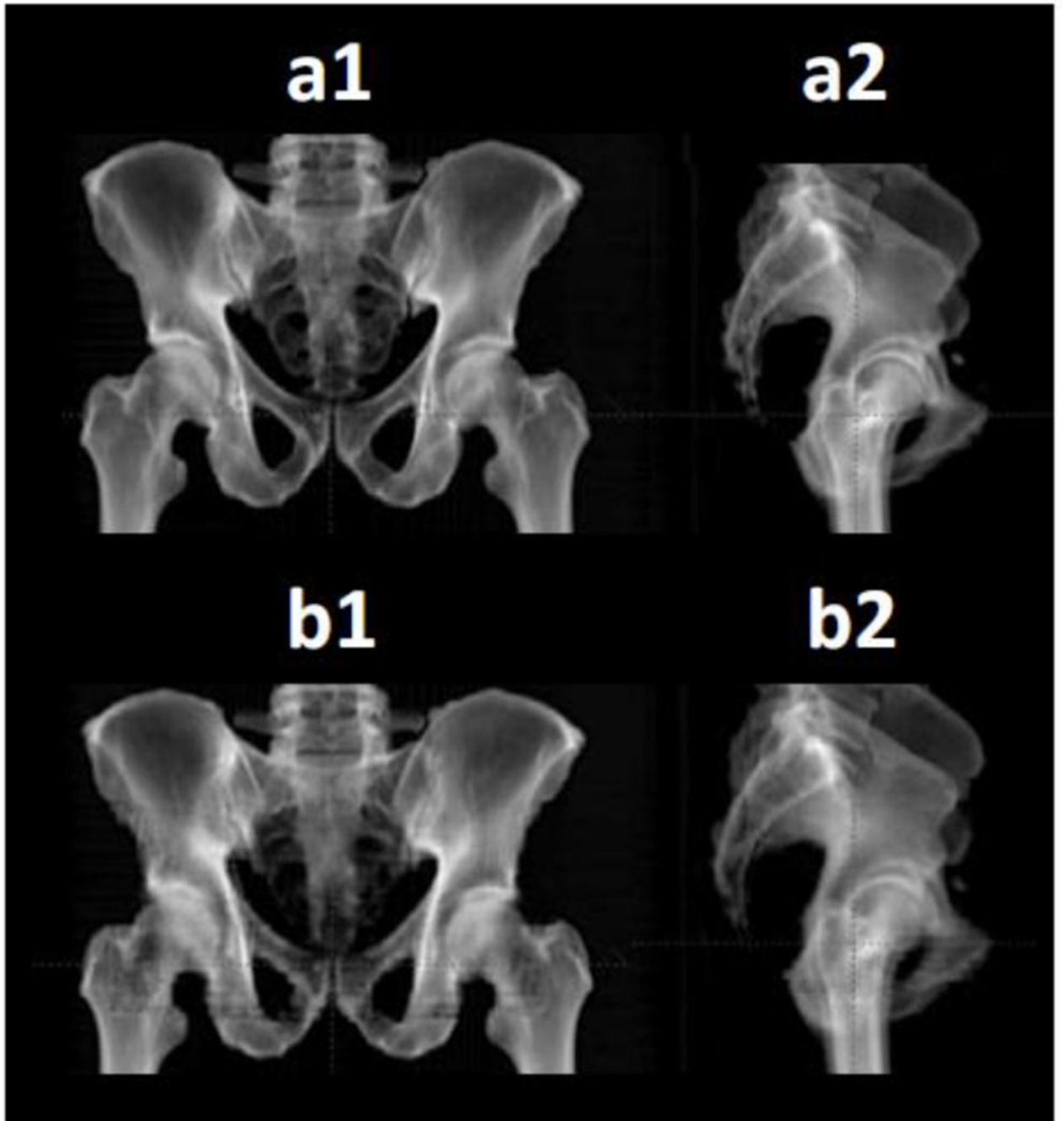


Figure 7.
The anteroposterior (AP) and lateral DRRs constructed from (a) pCT, and (b) SCT of the patient in Figure 2.

Table I.

Differences in DVH metrics of PTVs and OARs among all 17 plans.

PTV	Dmin	D10	D50	D95	Dmean	Dmax
Mean	-0.088	-0.053	-0.058	-0.059	-0.057	-0.062
STD (Gy)	0.135	0.051	0.050	0.055	0.050	0.099
Relative Mean	-0.233	-0.121	-0.133	-0.141	-0.133	-0.152
STD (%)	0.356	0.136	0.140	0.141	0.136	0.238
P-Value	0.987	0.993	0.992	0.992	0.992	0.992
Bladder	Dmin	D10	D50	D95	Dmean	Dmax
Mean	-0.008	-0.081	-0.039	-0.009	-0.042	-0.088
STD (Gy)	0.017	0.052	0.038	0.013	0.033	0.072
Relative Mean	-0.058	-0.184	-0.198	-0.081	-0.184	-0.187
STD (%)	0.350	0.145	0.178	0.280	0.150	0.183
P-Value	0.996	0.988	0.991	0.997	0.989	0.988
Rectum	Dmin	D10	D50	D95	Dmean	Dmax
Mean	0.001	-0.055	-0.027	-0.001	-0.027	-0.072
STD (Gy)	0.006	0.066	0.047	0.015	0.048	0.088
Relative Mean	0.166	-0.135	-0.104	0.040	-0.116	-0.154
STD (%)	0.415	0.162	0.237	0.413	0.190	0.226
P-Value	0.998	0.993	0.993	0.999	0.993	0.990
Penile Bulb	Dmin	D10	D50	D95	Dmean	Dmax
Mean	-0.026	-0.014	-0.003	-0.006	-0.007	-0.032
STD (Gy)	0.055	0.033	0.018	0.012	0.017	0.057
Relative Mean	-0.259	-0.064	-0.047	-0.084	-0.065	-0.090
STD (%)	0.421	0.129	0.214	0.194	0.153	0.140
P-Value	0.987	0.998	0.999	0.998	0.998	0.995
Right Femur	Dmin	D10	D50	D95	Dmean	Dmax
Mean	-0.001	-0.014	-0.003	0.001	-0.005	-0.016
STD (Gy)	0.003	0.016	0.011	0.004	0.011	0.032
Relative Mean	-0.090	-0.085	-0.058	0.101	-0.069	-0.066
STD (%)	0.363	0.109	0.145	0.272	0.132	0.143
P-Value	0.994	0.995	0.998	0.996	0.997	0.997
Left Femur	Dmin	D10	D50	D95	Dmean	Dmax
Mean	0.000	-0.018	-0.007	0.001	-0.008	-0.011
STD (Gy)	0.002	0.013	0.007	0.004	0.008	0.043

PTV	Dmin	D10	D50	D95	Dmean	Dmax
Relative Mean	0.013	-0.108	-0.082	0.049	-0.087	-0.071
STD (%)	0.282	0.083	0.089	0.287	0.087	0.174
P-Value	0.999	0.994	0.997	0.997	0.996	0.998

Author Manuscript

Author Manuscript

Author Manuscript

Author Manuscript